



## Article

# Characterization of calcined red soil applied in the removal of methylene blue dye from wastewater to produce a hybrid pigment

Daiane L. Silva, Nayara Balaba, Dienifer F.L. Horsth, Silvia Jaerger  and Fauze J. Anaisi 

Universidade Estadual do Centro-Oeste, Departamento de Química, Laboratório de Materiais e Compostos Inorgânicos, Alameda Élio Antonio Dalla Vecchia, Guarapuava, PR, Brazil

### Abstract

We obtained natural red soil (RS), rich in iron, from the region of Palotina in the state of Paraná, Brazil. The RS sample was purified by suspension in water and sieved to remove plant particulates. It was then treated thermally at 800°C to remove organic volatiles; this sample was called RS800. The samples were characterized using X-ray diffraction, X-ray fluorescence, infrared and electronic spectroscopy,  $\zeta$ -potential analysis and scanning electron microscopy. Colorimetric studies were performed according to the CIEL\*a\*b\* system. Tests have shown that RS800 has the ability to remove methylene blue (MB) dye from wastewater. Thus, it was used as an adsorbent at various temperatures (25, 35, 45°C). According to the Langmuir model, the maximum adsorption capacity ( $q_{\max}$ ) was 23.256 mg g<sup>-1</sup> (25°C). Unexpectedly, increasing temperature reduced  $q_{\max}$  to 21.659 mg g<sup>-1</sup> at 35°C and to 21.186 mg g<sup>-1</sup> at 45°C. Therefore, RS800 must be used at room temperature (25°C), making its application in large-scale wastewater treatment feasible. After using RS800 as an adsorbent, the solids were filtered, dried, pulverized, and used as hybrid pigments in commercial white paints. Pigmented paints were used to paint a plaster specimen and colorimetric measurement was performed. These paints were tested for colour stability in acidic and alkaline environments. The results indicate that RS800 is efficient in the treatment of water contaminated with cationic dyes and can be reused as a hybrid pigment.

**Keywords:** Adsorption, cationic dye, hybrid pigment, red soil, wastewater treatment

(Received 7 February 2023; revised 14 May 2023; Accepted Manuscript online 5 June 2023; Associate Editor: Professor Chun Hui Zhou)

Due to the modern phenomenon of so-called ‘fast fashion’, the textile industry has burgeoned. This relies on the rapid manufacture and increased consumption of short-duration clothing. With the help of the internet, there has been an increase in the speed of purchasing clothing items *via* e-commerce (Niinimäki *et al.*, 2020). As a result, the excessive consumption of such clothing has had significant environmental impacts, such as water pollution from discarded textile waste containing organic chemicals, among them organic dyes that have toxic effects on the environment (Aksu, 2005). In addition to dyes, other pollutants contained in wastewater include chemical contaminants such as heavy metals, organic and inorganic particles, toxins, pharmaceuticals, hormones and other hazardous substances, and biological pollutants such as bacterial species and viruses, worms and/or algae can also be present in large quantities (Nayl *et al.*, 2023). As a result, degradation of the organic material in water has occurred.

Within this context, synthetic dyes are also used widely in the paper, plastic, leather, pharmaceutical, cosmetics and food industries (Aksu, 2005; Rodrigues *et al.*, 2020). In general, dyes are classified as anionic or cationic based on their chemical functionality, and they are highly toxic and harmful to humans and the

environment (Munir *et al.*, 2020) when industrial effluents contain concentrations of such dyes that are greater than allowed limits. Because there is no specific legislation that establishes colour standards for effluents in Brazil, such standards must be adopted; for freshwater bodies, the tolerable value of real or true colour is up to 75 mg Pt L<sup>-1</sup> (Conama, 2005). Therefore, effluents need to be treated before being discharged into aquatic environments (Aksu, 2005; Conama, 2005; Rodrigues *et al.*, 2020).

Colour is one of the first results of contamination that can be observed by the human eye (Aksu, 2005). From an aesthetic point of view, colour removal can be considered very important because it is associated directly with public perceptions of water quality (Pereira & Alves, 2012). Among the organic dyes used in the textile industry, methylene blue (MB; 3,7-bis(dimethylamino) phenothiazine chloride tetramethylthionine chloride) is a cationic dye used in the dyeing of cotton and wool fabrics, presenting in its structure (–N=N–) groups linked to aromatic systems, giving it great chemical stability (Honorato *et al.*, 2015). When MB is released in rivers and lakes, it decreases the passage of solar radiation, reducing natural photosynthetic activity and causing changes in aquatic biota (Honorato *et al.*, 2015).

MB has been found have some medicinal effects when used appropriately as opposed to ingestion *via* contaminated water. For example, it can be used to treat vasoplegia after transplant operations, to treat malaria at a treatment dosage of 36–72 mg kg<sup>-1</sup> over 3 days and in the neutralization of heparin (Oladoye *et al.*, 2022). However, the release of untreated dye-laden wastewater can lead to many health risks. For example, in

**Corresponding author:** Fauze J. Anaisi; Email: [anaissi@unicentro.br](mailto:anaissi@unicentro.br)

**Cite this article:** Silva DL, Balaba N, Horsth DFL, Jaerger S, Anaisi FJ (2023). Characterization of calcined red soil applied in the removal of methylene blue dye from wastewater to produce a hybrid pigment. *Clay Minerals* 58, 83–94. <https://doi.org/10.1180/clm.2023.13>

humans, MB dye can induce various diseases, such as cyanosis, tissue necrosis, the formation of Heinz bodies, vomiting, jaundice, shock, increased heart rate, *etc.* (Alver *et al.*, 2020; Oladoye *et al.*, 2022).

Various techniques for dye removal can be found in the literature, among them coagulation/flocculation and electron beam irradiation (Anvari *et al.*, 2014), ozonation (Zhao *et al.*, 2004), electrolysis (Wang, 2009), photocatalysis and electrochemical approaches (Anantha *et al.*, 2020) and adsorption (Almeida *et al.*, 2009). Adsorption is one of the most efficient and advantageous of these techniques due to its simplicity, low cost and use of various adsorbents (Moreira *et al.*, 2009; Shen *et al.*, 2009). Several sorbents are used for the adsorption of dyes and other contaminants in aqueous media, the most pertinent being activated carbon, which is expensive and is only available in limited quantities. Some alternative and sustainable sorbents have been employed, such as agricultural residues and bagasse. However, these biosorbents need to undergo a series of physical and chemical modifications to improve their efficiency, including burning, grinding and acidic or alkaline activation, and their quantities are also limited (Munir *et al.*, 2020). In the studies by Hameed *et al.* (2007), bamboo was used to prepare activated carbon *via* physicochemical activation with potassium hydroxide (KOH) and carbon dioxide (CO<sub>2</sub>) as activating agents at 850°C for 2 h. Similarly, in the report by Benhachem *et al.* (2019) for the activation of starch-activated carbon, in addition to calcination at 500°C for 2 h, high concentrations of NaOH for activation, several steps of washing with HCl and oven drying were also used. These are all processes that increase the cost and difficulty of preparing such adsorbents.

Brazil contains large volumes of soils with significant iron oxide contents. Depending on the region and the iron level, these soils can be classified as Latosols, Argissols, Cambissolos, Chernossolos or Nitossolos (Ker, 1997). The main activities of iron oxides present in soils are related to the retention of pollutants (heavy metals) and the fixation of phosphorus in soils, making this nutrient unavailable to plants and affecting soil cation-exchange capacity (dos Santos & Zaroni, 2021). The most common phases found are hematite and goethite, which are responsible for the red and yellow colours of these soils, respectively (Bortoluzzi *et al.*, 2007). In highly weathered soils of tropical and subtropical regions, such as those where Brazil's Latosols are found, goethite and hematite are the dominant iron oxides, being related to the evolution of these soils (Ker, 1997).

Within these circumstances, the iron oxides, hydroxides and oxyhydroxides comprise a group of minerals that have received increasing attention from the scientific community because they can interact with pollutants due to specific aspects of their crystal

chemistry or participate in various reactions as sorbents or oxidant reducers (Melo & Alleoni, 2009). These iron oxides are found among the main components of the clay fractions of highly weathered soils. They are often dispersed in the soil solution as fine particles of varying degrees of crystallinity covering the clay minerals or in the form of organic complexes (Ker, 1997). These iron oxides together with clay minerals can be applied in the treatment of aqueous solutions of MB, making them an excellent choice for the sorption process because they are abundant, low cost and classified as environmentally friendly materials. Therefore, they could replace low-performance biosorbents and expensive activated carbons in the sorption process (Gonçalves *et al.*, 2009).

Within this context, various new adsorbents have been tested to help with the control of pollutants. In this study, a reddish soil was heat-treated for use as a low-cost adsorbent to remove MB from an aqueous solution. This study also highlights the use of the residue generated during the adsorption process as a pigment for dispersion in paint.

## Materials and methods

### Purification and thermal treatment of the adsorbent

The adsorbent material, a reddish soil (Fig. 1a), was soil collected in the region of Palotina, PR, Brazil (24°17'46"S, 53°50'35"W). First, the soil was purified by placing it in drinking water and shaking it mechanically for 24 h to achieve total dispersion. Then, this dispersion was sieved through a coarse mesh sieve for domestic use to remove fibrous material and debris. The sieved suspension was kept at rest for 24 h, and then the first wash was performed, which consisted of adding water to cover two-thirds of the material, stirring for ~20 min and leaving it to decant for 24 h. After decanting, the water was removed before another wash was performed. After three decanting steps, the suspension was filtered through a porous plate funnel (number 4). The red mass obtained was dried in an oven at 80°C for 24 h. Then, it was pulverized in a pestle and mortar set and sieved through a stainless steel sieve (250 µm and 65 mesh). The reddish soil was separated into two parts (Fig. 1), one part being the raw red soil (RS) and the other part being calcined at 800°C for 60 min (ramp of 10°C min<sup>-1</sup>). The latter sample was called RS800.

### Quantification of MB dye

The MB solutions were quantified from a calibration curve according to the Lambert–Beer law using an ultraviolet–visible (UV–Vis) spectrophotometer (Shimadzu UV-1800) in the spectral range 400–800 nm with a wavelength of 665 nm. A stock

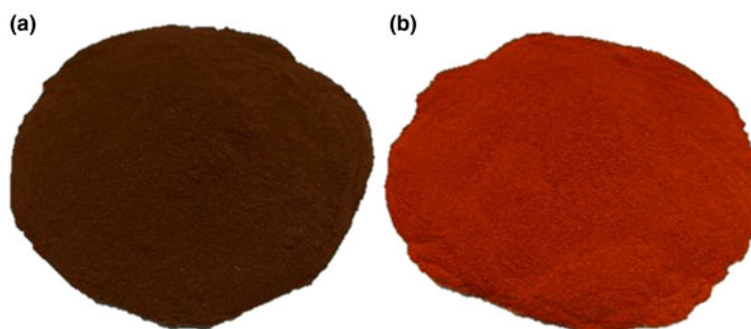


**Figure 1.** Photographic images of (a) RS and (b) RS800.

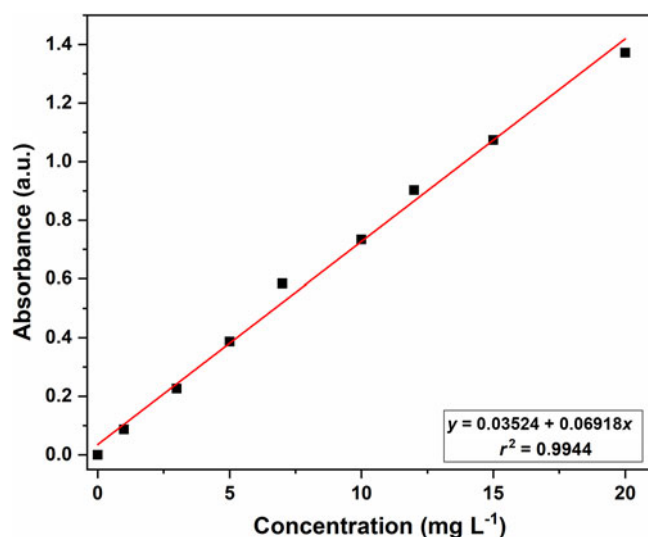


Figure 2. Calibration curve for MB dye.

standard solution of MB of concentration 1000 mg L<sup>-1</sup> was prepared, from which dilutions were made to obtain the other curves in the construction of the calibration curve (Fig. 2).

### Characterization techniques

The determination of the  $\zeta$ -potential was performed according to an adaptation of the methodology of Lima *et al.* (2000). The adsorbent potential was measured before the adsorption process using 1 mg of material dispersed in 1 mL of 10<sup>-2</sup> mol L<sup>-1</sup> NaCl solution. The suspensions were placed in an ultrasonic bath for 8 min and left to rest for 15 min. The  $\zeta$ -potential was measured as a function of pH variation between 2 and 12. The pH adjustment between 2 and 12 was performed by adding hydrochloric acid (HCl; 0.1 mol L<sup>-1</sup>) and sodium hydroxide (NaOH; 0.1 mol L<sup>-1</sup>). The  $\zeta$ -potential measurements were performed using ZETASIZER Malver equipment (NANO ZS90 model), and the correlation between clay mass and solution volume was the same for all points on the curve at 1 mg mL<sup>-1</sup>.

The samples were characterized in terms of their composition using energy-dispersive X-ray fluorescence spectroscopy (EDXRF). The analysis was performed using a Shimadzu model EDX-700HS, with an acquisition time of 60 s per analytical channel, a vacuum atmosphere and a 10 mm collimator. The crystalline phases were identified using powder X-ray diffraction (XRD) with a Bruker model D2 Phaser using Cu-K $\alpha$  radiation ( $\lambda = 1.5418 \text{ \AA}$ ), scanning over 2–50°2 $\theta$  at a step rate of 0.2° s<sup>-1</sup>, a power of 300 W, a voltage of 30 kV and a current of 10 mA. The average size of crystallites was calculated using the Scherrer equation (Cullity & Stock, 1956), and basal spacing values were calculated using the Bragg equation (Cullity & Stock, 1956). The morphologies of the RS and RS800 particulate samples were examined using scanning electron microscopy (SEM-VEGA 3, TESCAN). For the analysis, each sample was placed on carbon tape. The samples were gold-coated to make their surfaces conductive. Fourier-transform infrared spectroscopy (FTIR) analyses were performed using a PerkinElmer Frontier spectrometer in the 4000–650 cm<sup>-1</sup> region, and eight scans were performed with a resolution of 2 cm<sup>-1</sup>. FTIR spectra

were obtained in attenuated total reflectance (ATR) acquisition mode using a high-capacity ZnSe crystal. The electronic spectra of the powdered samples were measured in the range of 400–900 nm using a UV-Vis Ocean Optics spectrophotometer (model USB-2000) in absorbance mode. The colorimetric measurements (CIEL\*a\*b\*<sup>\*</sup>; Quindici, 2013) were performed on pigments in powder form, and after application to a test specimen of plaster, the pigments were dispersed in a proportion of 5% (w/w) in commercial white paint. According to this method, L\* is the colour lightness, ranging from black (L\* = 0) to white (L\* = 100), a\* is the green (-)/red (+) axis and b\* is the blue (-)/yellow (+) axis (Quindici, 2013).

### Adsorption studies

MB removal assays were performed with aqueous solutions containing 100–225 mg L<sup>-1</sup> of the dye. Flasks containing 30 mL of dye were placed under magnetic stirring in a thermal bath at 25, 35 and 45°C for 30 min. Thereafter, 500 mg of RS800 was added, and the system was kept under constant magnetic stirring and controlled temperature for 60 min. Aliquots of the supernatant were analysed in a spectrophotometer in the wavelength range of 400–800 nm before and after adsorption to evaluate the performance of the adsorbent. The RS800 samples collected after the adsorption assays were used as pigments. The amount of MB adsorbed and the percentage of dye removed were calculated using Equations 1 and 2, respectively:

$$q = \frac{(C_0 - C_f)}{m} \times V \quad (1)$$

$$\% \text{ removal} = 100 \times \frac{(C_0 - C_f)}{C_0} \quad (2)$$

where  $q$  is the amount of dye adsorbed by the adsorbent (mg g<sup>-1</sup>),  $C_0$  is the initial dye concentration (mg L<sup>-1</sup>) in contact with the adsorbent,  $C_f$  is the dye concentration (mg L<sup>-1</sup>) after the process of adsorption,  $m$  (g) is the mass of the adsorbent and  $V$  (L) is the volume of the solution.

### Pigment dispersion in commercial paint

The materials from the adsorption process were used in 5% (w/w) dispersions in white paint. The procedure consisted of spraying the pigment and then homogenizing it in white paint for coating plaster blocks in a single coat to simulate its application in buildings.

### Colour stability

Colour stability tests were performed in acidic and alkaline environments using desiccators to control the experimental environment. Petri dishes containing HCl and NaOH were placed in different desiccators to reproduce the acidic and alkaline environments, respectively (Horsth *et al.*, 2021). The paints that were used to coat the plaster blocks were added to the desiccators, which were then sealed. Colorimetric measurements were performed before the test and after 72 h to verify the colorimetric stability of the pigments.

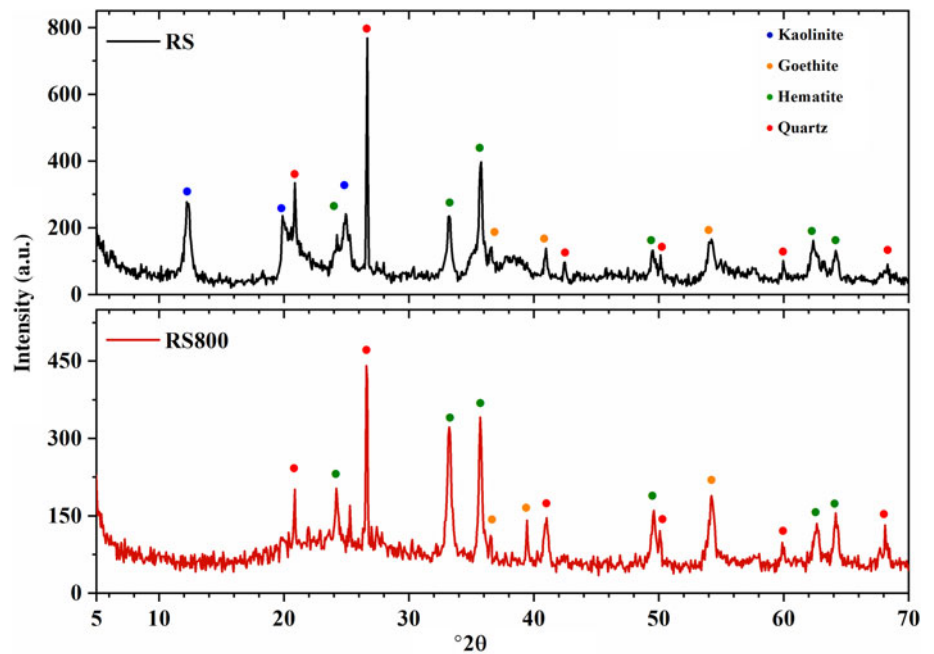


**Figure 3.** XRD traces of samples RS and RS800.

## Results and discussion

### Mineralogical analysis: constituent phases (XRD) and chemical analysis (EDXRF)

The XRD traces (Fig. 3) show the main constituent phases of soil identified for samples RS and RS800. The XRD trace of the RS sample shows peaks related to the kaolinite phase, identified by the presence of the peak  $12.4^{\circ}2\theta$  corresponding to the basal spacing with a value of  $7.28 \text{ \AA}$ , and the other peaks indicating this phase are  $19.9$  and  $24.9^{\circ}2\theta$  (Bortoluzzi *et al.*, 2007). Kaolinite exists in soil samples from various places around the world, including soils from southern Brazil, and it is reported very frequently. The great abundance of this clay mineral in Brazilian soils is due to the country's environmental conditions. As Brazil is a tropical country, a hot and humid climate predominates and, in association with the acidic environment of the soil, this favours the alteration of a considerable amount of primary minerals such as feldspars and micas or of secondary minerals degrading clays of the 2:1 type. Kaolinite is a phase that has been found in clay fractions of soils containing various materials from various geological periods (Ker, 1997; Bortoluzzi *et al.*, 2007). After calcination at  $800^{\circ}\text{C}$ , the XRD trace of sample RS800 shows changes in the interlamellar layers of its clay fraction, evidence of which is the disappearance of the kaolinite peaks, as kaolinite loses its hydroxyls at high temperatures, contributing to the degradation of the structure of this phase (Moraes *et al.*, 2003; Bortoluzzi *et al.*, 2007). In addition to kaolinite, the phases quartz ( $\text{SiO}_2$ ), goethite ( $\text{FeO}(\text{OH})$ ) and hematite ( $\text{Fe}_2\text{O}_3$ ) were identified in the RS sample. These iron oxides are dominant in soils with a high degree of weathering, called Latosols, from tropical and subtropical regions (Ker, 1997; Inda Junior & Kämpf, 2005), and even after the calcination of RS there were no structural changes to these phases. From this analysis, great concentrations of Si, Al and Fe ions were identified due to the kaolinite, goethite and hematite phases identified using XRD (Fig. 3). The chemical compositions of the qualitatively analysed samples are shown in Table 1.

In the RS sample, the presence of silicon dioxide ( $\text{SiO}_2$ ) was substantial, in addition to aluminium oxide ( $\text{Al}_2\text{O}_3$ ) and iron

oxide ( $\text{Fe}_2\text{O}_3$ ). These components are due to the presence of varying amounts of kaolinite, gibbsite, goethite and hematite, and there were lesser proportions of other components in the clay fraction of the soil. A high aluminium oxide content is common because gibbsite is a significant mineral in soil, along with quartz, representing the silicon dioxide fraction. Quartz is one of the most resistant and abundant primary minerals in the rocks of the Earth's crust, and soils derived from rocks containing quartz and iron minerals are considered much more evolved (*i.e.* they will have an advanced pedogenetic degree; Ker, 1997).

Iron components include oxides, hydroxides and oxyhydroxides, which are among the main components of the clay fraction and are found dispersed in the soil mass in the form of organic complexes or particles containing clay minerals. A high titanium content is also characteristic of the region's soils (Ker, 1997). It was also observed that thermal treatment did not alter the sample constituents significantly.

### Colorimetric measurements (CIEL\*a\*b\*)

The thermal treatment of the RS sample promoted a color change. This indicates the importance of carrying out colorimetric measurements to verify the difference in color ( $\Delta E$ ) between the RS and RS800 samples. The  $\Delta E$  value refers to the comparison between colours, and the total colour variation was calculated using Equation 3 in *ColorMine* software (Horsth *et al.*, 2021):


$$\Delta E = \sqrt{(\Delta L^*)^2 + (\Delta a^*)^2 + (\Delta b^*)^2} \quad (3)$$

**Table 1.** Chemical compositions of samples RS and RS800.

Sample	$\text{SiO}_2$	$\text{Al}_2\text{O}_3$	CaO	$\text{Fe}_2\text{O}_3$	$\text{K}_2\text{O}$	$\text{TiO}_2$	Others
RS	37.07	23.81	0.81	31.75	0.20	5.02	1.30
RS800	37.50	25.65	0.81	29.71	0.21	5.02	1.07



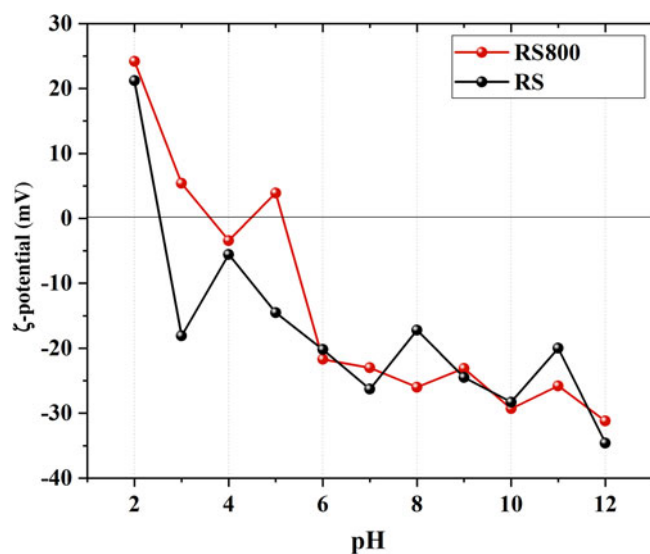
**Table 2.** Colorimetric parameters of samples RS and RS800.

Sample	Colorimetric parameters					$\Delta E$	Photograph
	L*	a*	b*	C*	h*		
RS	17.86	15.87	17.75	23.81	48.20	4.77	
RS800	19.78	19.84	19.58	27.88	44.62		

The colour difference obtained between the two samples was 4.77, which is considered a very clear difference (Quindici, 2013). The colorimetric parameters of the RS and RS800 samples are shown in Table 2. The L\* parameter is the brightness of the colour, and the most luminous sample is RS800, while the RS sample is the least luminous. The parameters a\* and b\* refer to the chromaticity (C\*) of the samples, where a\* represents the variation from red to green, with (+)a\* tending to red and (-)a\* tending to green. The b\* parameter indicates the variation from blue and yellow, with (+)b\* tending to blue and (-)b\* tending to yellow (Horsth *et al.*, 2021). In this case, the heat treatment caused an increase in the values of the coordinates a\* and b\*, with both remaining positive and in the red and yellow colour quadrants, rendering the sample redder. This behaviour is observed due to goethite undergoing dehydroxylation and forming hematite at temperatures >200°C, the latter of which has a red colour (Oliveira *et al.*, 2013).

### $\zeta$ -potential

The clay fraction of the soil showed a pH-dependent surface charge (Fig. 4). Tropical soils are abundant in kaolinite, iron oxide and aluminium oxide, producing a variable surface electrical charge due to the surface hydroxylation of soil colloids. The hydroxyl groups of these minerals can be linked to one, two or three metals in the mineral structure, so positive and

**Figure 4.**  $\zeta$ -potential as a function of pH for RS and RS800.

negative charges can be created in this hydroxylated layer, protonating or deprotonating the molecules within the mineral (Fontes *et al.*, 2001).

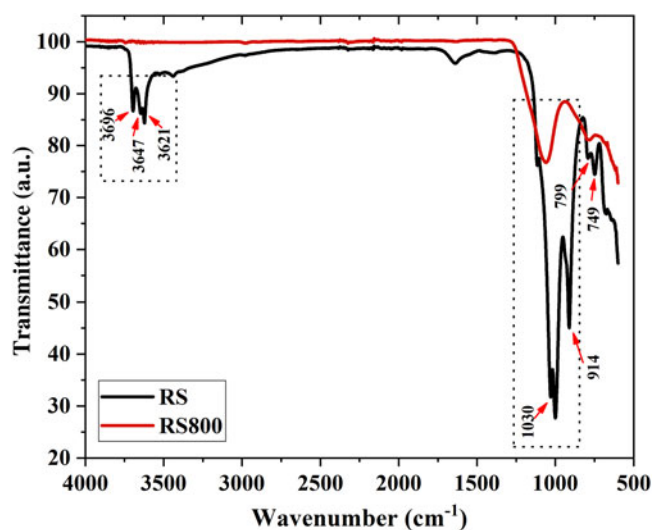
In a very acidic environment (pH 2), the soil had a positive surface charge, ranging from +21.2 mV for RS to +24.2 mV for RS800, due to the protonation of the hydroxyl groups of the iron and aluminium oxides (Fontes *et al.*, 2001). As the pH increased to pH 4, deprotonation of the hydroxyl groups occurred for both samples, generating negative surface charges that remained unchanged until pH 12. For the RS sample, the charge was more negative, with a  $\zeta$ -potential of -34.6 mV at pH 12.

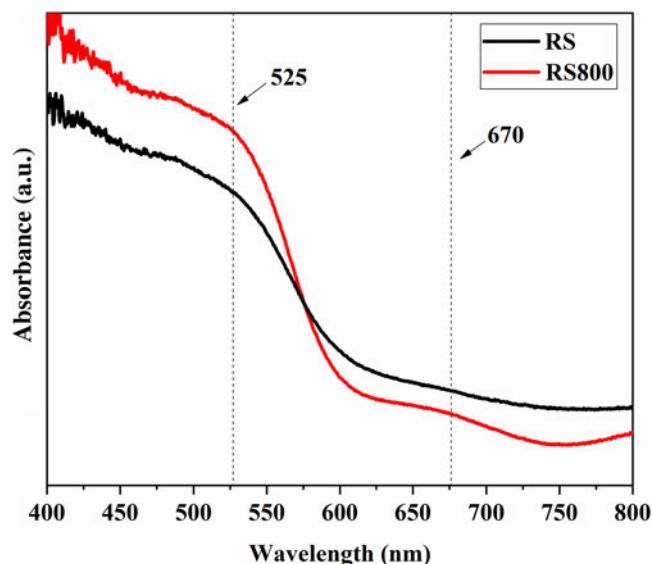
### Vibrational spectroscopy (FTIR)

Figure 5 shows the FTIR spectra for RS and RS800. The main difference between the spectra before and after calcination relates to the shape of the bands after the calcination process, as the RS sample showed typical kaolinite bands with well-defined peaks at 3696 cm<sup>-1</sup> (O–H axial deformation in kaolinite), 3647 cm<sup>-1</sup>, 3621 cm<sup>-1</sup> (O–H axial strain in kaolinite), 1030 cm<sup>-1</sup> (Si–O axial deformation in kaolinite) and 914 cm<sup>-1</sup> (O–H angular deformation in kaolinite), characteristics that are shared by similar spectra found in the literature (Benites *et al.*, 1999; Gonçalves *et al.*, 2008; Kumar & Rajkumar, 2014). The band at 799 cm<sup>-1</sup> (Si–O–Si vibrations) refers to quartz. The vibration mode at 749 cm<sup>-1</sup> indicates the presence of hematite (Fe–O; Martinelli *et al.*, 2014). In the spectrum of the RS800 sample, changes in the band profile can be observed. Due to the thermal treatment of the sample, the bands that identify kaolinite disappeared, which corroborates the XRD results.

### Absorption spectroscopy

Figure 6 shows the electronic absorbance spectra in the visible region for the RS and RS800 samples. A band at 525 nm was identified for both samples, the absorbance of which indicates a double-excitation process related to the electronic transition <sup>6</sup>A<sub>1</sub>(<sup>6</sup>S)–<sup>6</sup>A<sub>1</sub>(<sup>6</sup>S) → <sup>4</sup>T<sub>1</sub>(<sup>4</sup>G)–<sup>4</sup>T<sub>1</sub>(G), which is responsible for the reddish colour of the hematite phase (Horsth *et al.*, 2021). A band at 670 nm was identified only for the RS800 sample, and

**Figure 5.** FTIR spectra for samples RS and RS800.



**Figure 6.** Absorbance spectra in the visible region for samples RS and RS800.

this band can be associated with the  $\text{Fe}^{3+}$  ion in an octahedral coordination in the electronic transition  ${}^6\text{A}_{1g} \rightarrow {}^4\text{T}_{2g}$  (Gargori *et al.*, 2012).

Figure 7 shows the linear extrapolation of the curves obtained from the reflectance spectra of the RS and RS800 samples, which represents the estimated value for the band gap ( $E_{\text{gap}}$ ) obtained using the direct Kubelka–Munk method (Morales-Marín *et al.*, 2019). The direct gap is the one in which the maximum energy of the valence band coincides with the lowest-energy wave vector of the conduction band (Borth *et al.*, 2021). Band gap values of 1–3 eV correspond to semiconductor materials, and the calculated data confirm the semiconductor nature of the iron oxides existing in the soil samples before and after calcination (Deotale & Nandedkar, 2016). The energy variation between the two samples was  $\Delta E_{\text{band gap}} = -0.01$  eV.

### Surface morphology (SEM)

SEM images of the raw soil sample and after thermal treatment are shown in Fig. 8. The RS sample (Fig. 8a,b) shows a

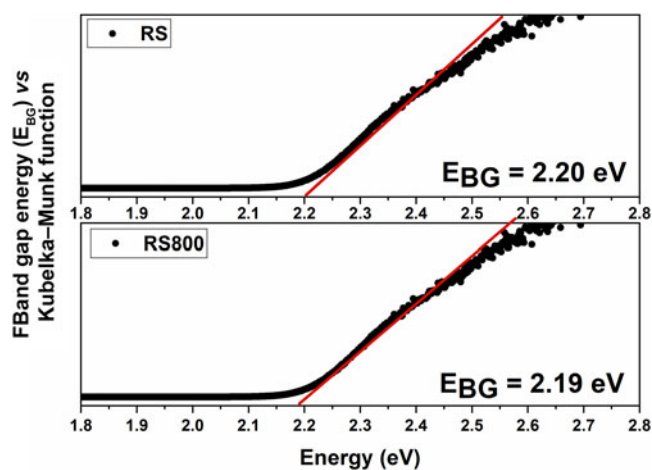


**Figure 7.** Band gap energy estimations of samples RS and RS800. Red lines represent the linear extrapolations for calculating the band gaps of the samples.

disorganized morphology with varied and overlapping shapes of various sizes, a morphology that is similar to kaolinite (Xu & Van Deventer, 2002), corroborating the XRD data. After thermal treatment, the RS800 particles (Fig. 8c,d) in the sample became more compact and defined as pseudospheres of irregular size, demonstrating the loss of the kaolinite phase after calcination at 800°C (Morales *et al.*, 2003).

### MB adsorption isotherms using RS800

Figure 9 presents the MB removal percentage *via* adsorption with RS800 at 25, 35 and 45°C at various initial MB concentrations. The results show that the percentage removal of MB increases as the initial concentration decreases. However, more ions of MB dye were retained by RS800 when the initial MB concentration increased. This result supports the findings of the great adsorption capacity of RS800. When the mass of the adsorbent is fixed and the amount of adsorbate (MB) increases, the adsorption sites become occupied until achieving saturation of the surface layer.

The determination of the equilibrium conditions between the solute concentration in the solution and the adsorbed phase is crucial for the appropriate design and operation of an adsorption process (Meili *et al.*, 2019). A correct modelling analysis is fundamental for managing adsorption processes as it can enable the accurate determination of the performance of such systems (Meili *et al.*, 2019). In this study, the data regarding the adsorption of MB dye onto RS800 were adjusted according to Langmuir, Freundlich and Temkin isotherm models, and their correlation parameters are presented in Fig. 10 & Table 3.

For systems that follow the assumption of ideal homogeneous surface adsorption, the Langmuir model is applicable. This model also considers that the adsorption energy is constant and does not depend on the degree of adsorbent-site occupation (Meili *et al.*, 2019). Therefore, the Freundlich model fits better for multilayer adsorption with non-uniform energy distribution and a heterogeneous system (Meili *et al.*, 2019). The Temkin model assumes a uniform distribution of bonding energy up to some maximum bonding energy level (Inyinbor *et al.*, 2016). This model ignores extremely low and high concentrations and assumes that any decrease in adsorption heat is linear (Inyinbor *et al.*, 2016; Bingül, 2022).

The Langmuir isotherm in its linear form is usually given as Equation 4:

$$\frac{C_e}{q_e} = \frac{1}{q_{\text{max}}K_L} + \frac{C_e}{q_{\text{max}}} \quad (4)$$

where  $C_e$  is the dye concentration dye at equilibrium ( $\text{mg L}^{-1}$ ),  $q_e$  ( $\text{mg g}^{-1}$ ) is the amount of MB adsorbed per unit mass of RS800 at equilibrium,  $K_L$  ( $\text{L mg}^{-1}$ ) is the Langmuir constant related to the affinity of the binding sites and  $q_{\text{max}}$  ( $\text{mg g}^{-1}$ ) is a parameter related to the maximum amount of MB per unit weight of RS800.

The linearized form of the Freundlich isotherm is given as Equation 5:

$$\ln q_e = \ln K_F + \frac{1}{n} \ln C_e \quad (5)$$

where  $K_F$  ( $\text{mg L}^{-1}$ ) is the Freundlich constant and  $n$  is a parameter related to the intensity of adsorption and the heterogeneity of the

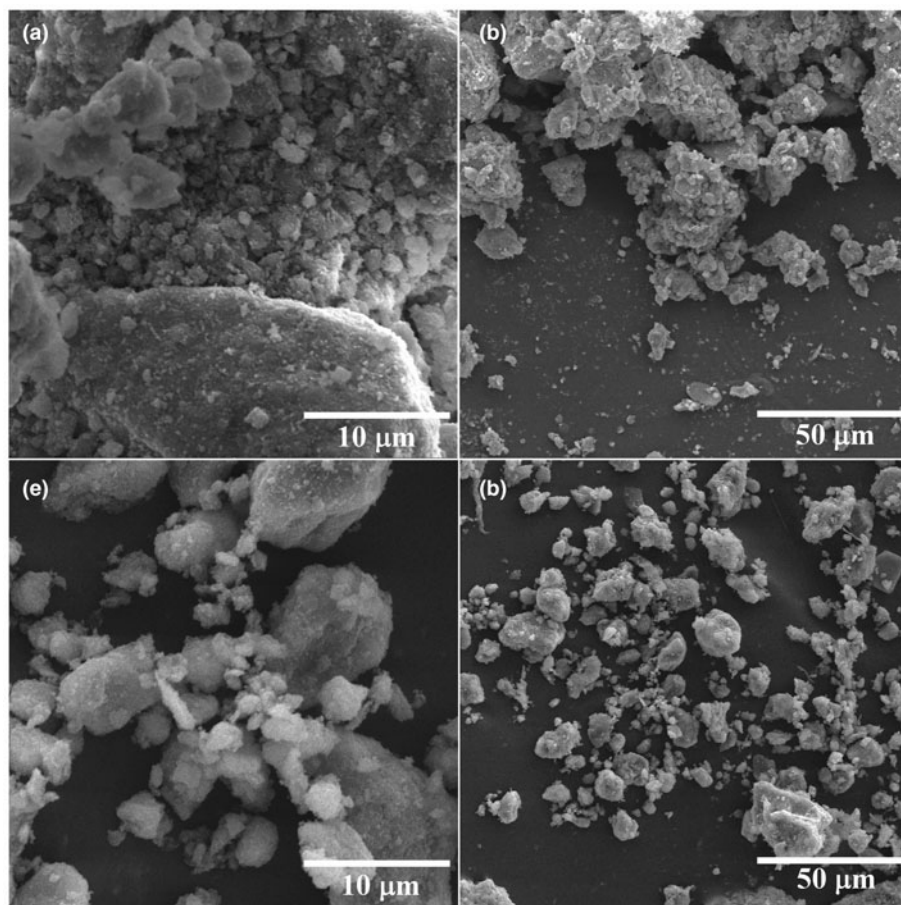


Figure 8. SEM images of the morphology of (a,b) RS and (c,d) RS800.

system.  $K_F$  and  $n$  are the Freundlich constants found from the intercept and slope of the straight line of the plot  $\ln q_e$  vs  $\ln C_e$ .

The Temkin model can be expressed as Equation 6:

$$q_e = \frac{RT}{b} \ln C_e + \frac{RT}{b} \ln K_T \quad (6)$$

where  $b$  is the Temkin isotherm of the heat of adsorption ( $J mol^{-1}$ ),  $T$  is the absolute temperature (K),  $R$  is the gas constant

( $8.314 J mol^{-1} K^{-1}$ ) and  $K_T$  is the Temkin equilibrium constant ( $L mg^{-1}$ ).

Figure 10 shows that the Langmuir isotherm curve is the most suitable isotherm curve for the experimental data, as has been observed previously (Bingül, 2022). Table 3 shows that the correlation coefficient ( $r^2$ ) obtained using the Langmuir isothermal model demonstrates a better fit ( $r^2 > 0.99$ ) than that obtained using the Freundlich model ( $r^2 < 0.99$ ). Therefore, the adsorption process of MB dye ions onto RS800 consists of monolayer

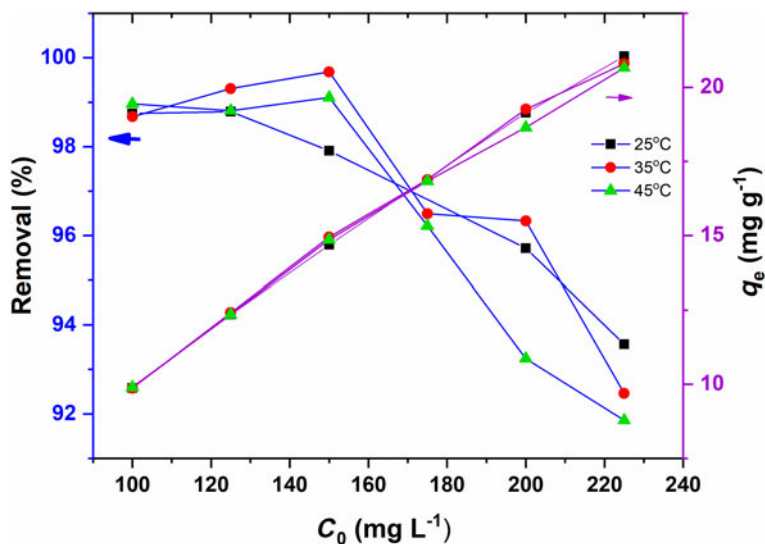
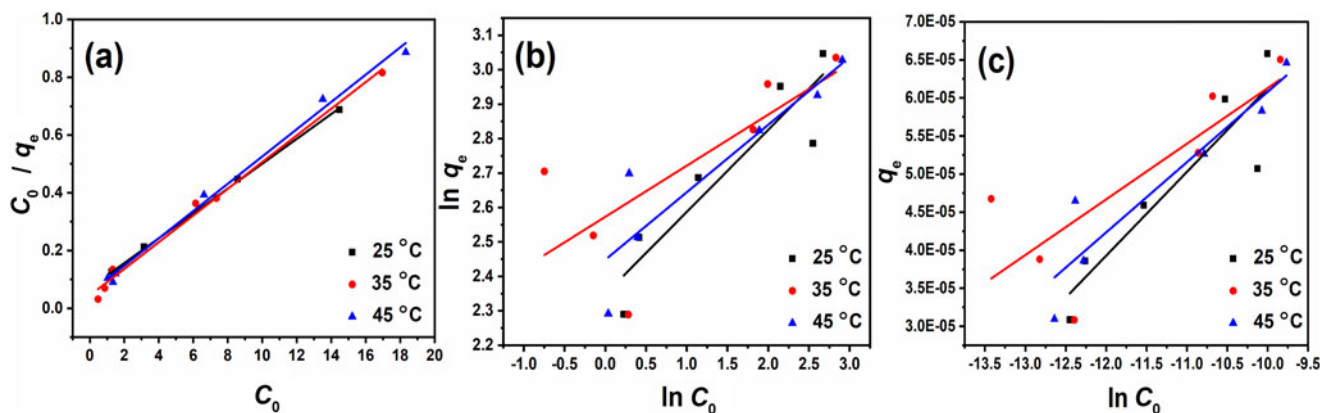


Figure 9. Experimental curves for the adsorption of MB dye onto RS800 at 25, 35 and 45°C.





**Figure 10.** Linear forms of (a) Langmuir, (b) Freundlich and (c) Temkin adsorption isotherms for the adsorption of MB dye onto RS800 at 25, 35 and 45°C.

adsorption with no significant interaction with neighbouring adsorbed molecules (Jaerger *et al.*, 2015; Meili *et al.*, 2019). The maximum adsorption capacity ( $q_{\max}$ ) is another important property that can be obtained using the Langmuir isotherm model, and its values were 23.256, 21.659 and 21.186 mg g<sup>-1</sup> for the RS800 at 25, 35 and 45°C, respectively.

The Freundlich isotherm considers an empirical relationship demonstrating the interaction between heterogeneous surfaces and adsorbate molecules (Bingül, 2022). Values of  $1/n$  from 0 to 1 indicate the degree of linearity between solution concentration and adsorption: the smaller the  $1/n$  value, the greater the expected heterogeneity (Bingül, 2022). The adsorption is considered chemical if  $n < 1$  and physical if  $n > 1$ . Table 3 shows that the  $1/n$  values were calculated as 4.192, 6.741 and 5.104 at 25, 35 and 45°C, respectively. These values are  $>1$ , indicating that the adsorbent is homogeneous. The  $n$  values were calculated as 0.239, 0.148 and 0.196 at 25, 35 and 45°C, respectively, indicating that the adsorption process is chemical.

The Temkin isotherm ignores extremely low and high concentrations and assumes a linear rather than a logarithmic decrease of the heat of adsorption (Inyinbor *et al.*, 2016). Table 3 shows that  $r_T^2$  is  $<0.99$ .

The thermodynamic parameters of an adsorption process such as the Gibbs free energy change ( $\Delta G^\circ_{\text{ads}}$ ), enthalpy change ( $\Delta H^\circ_{\text{ads}}$ ) and entropy change ( $\Delta S^\circ_{\text{ads}}$ ) show whether the process is endothermically favourable (Bingül, 2022). The parameters  $\Delta G^\circ_{\text{ads}}$ ,  $\Delta H^\circ_{\text{ads}}$  and  $\Delta S^\circ_{\text{ads}}$  were determined using Equations 7–9:

$$k_d = \frac{q_e}{C_e} \quad (7)$$

$$\ln k_d = \frac{\Delta H}{RT} + \frac{\Delta S}{R} \quad (8)$$

$$\Delta G^\circ = \Delta H^\circ - T\Delta S^\circ \quad (9)$$

where  $T$  is the adsorption temperature (K),  $R$  is the ideal gas constant (8.314 J K<sup>-1</sup> mol<sup>-1</sup>) and  $k_d$  is the distribution coefficient.

Figure 9 shows that increasing adsorption temperature does not have a significant effect on the removal capacity. Table 4 shows the thermodynamic data from this process. Sample RS800 showed a positive  $\Delta H^\circ_{\text{ads}}$  value, which indicates endothermic adsorption.  $\Delta H^\circ_{\text{ads}}$  values can also provide information regarding the mechanism of the adsorption process (Güleç *et al.*, 2022). The process is controlled by physical adsorption if its  $\Delta H^\circ_{\text{ads}}$  value ranges from 0 to  $-20$  kJ mol<sup>-1</sup>, or it will be a chemisorption process when it  $\Delta H^\circ_{\text{ads}}$  value ranges from  $-400$  to  $-80$  kJ mol<sup>-1</sup> (Chaari *et al.*, 2019). According to the isotherm discussion above, the adsorption of MB onto RS800 follows a chemisorption process.

The negative  $\Delta G^\circ_{\text{ads}}$  values observed indicate that this adsorption is a non-spontaneous process (Bingül, 2022). Additionally, Table 4 shows that increasing the adsorption temperature increases the  $\Delta G^\circ_{\text{ads}}$  value. This suggests that the process decreases in spontaneity at greater temperatures. Therefore, the adsorption process of MB onto RS800 becomes more favourable with decreasing temperature (Güleç *et al.*, 2022).

The negative  $\Delta S^\circ_{\text{ads}}$  values observable in Table 4 indicate a decrease of randomness at the solid–liquid interface during adsorption of MB onto RS800 (Chaari *et al.*, 2019). This result demonstrates the low affinity between the adsorbate MB molecules and the RS800 surface, which could explain the low values obtained for the adsorption capacity ( $q_{\max}$ ) observable in Table 3.

### Comparison with other adsorbents

Table 5 presents the adsorption capacities of other adsorbents regarding the adsorption of MB. As can be observed, the raw

**Table 3.** Parameters of the Langmuir, Freundlich and Temkin isotherms for the adsorption of MB dye onto RS800 at 25, 35 and 45°C.

Temperature (°C)	Langmuir			Freundlich			Temkin		
	$K_L$ (L mg <sup>-1</sup> )	$q_{\max}$ (mg g <sup>-1</sup> )	$r_L^2$	$K_F$ (L g <sup>-1</sup> )	$1/n$	$r_F^2$	$K_T$ (L g <sup>-1</sup> )	$b$ (J mol <sup>-1</sup> )	$r_T^2$
25	0.608	23.256	0.999	10.472	4.192	0.842	19.189	703.380	0.831
35	1.038	21.659	0.991	13.107	6.741	0.553	342.685	1095.379	0.632
45	0.880	21.186	0.994	11.571	5.104	0.825	54.334	895.165	0.876



**Table 4.** Thermodynamic parameters for the adsorption of MB dye onto RS800 at 25, 35 and 45°C.

T (°C)	$\Delta G^{\circ}_{\text{ads}}$ (kJ mol <sup>-1</sup> )	$\Delta S^{\circ}_{\text{ads}}$ (J K <sup>-1</sup> mol <sup>-1</sup> )	$\Delta H^{\circ}_{\text{ads}}$ (kJ mol <sup>-1</sup> )
25	19.177		
35	19.483	-30.674	10.036
45	19.790		

RS obtained in this study has a greater adsorption capacity value compared to the samples RS-TC and RS-HC (both samples of biochar produced from rapeseed, whitewood and seaweed) and sugarcane bagasse (Meili *et al.*, 2019; Güleç *et al.*, 2022). RS-TC and RS-HC had negative  $\Delta S^{\circ}_{\text{ads}}$  values that were very close to zero, indicating low affinity between the MB molecules and the adsorbent surface (Güleç *et al.*, 2022). Brown clay, natural clay and chemically modified lychee seed biochar had positive  $\Delta S^{\circ}_{\text{ads}}$  values, indicating the randomness at the solid-liquid interface during adsorption of MB onto these adsorbents due to the high affinity between the adsorbate molecules and the adsorbent surface (Munir *et al.*, 2020; Sahu *et al.*, 2020; Bingül, 2022). Therefore, in this study, it is observed that positive  $\Delta S^{\circ}_{\text{ads}}$  values can affect adsorption capacity directly, especially due to the low affinity between the MB molecules and raw RS surface.

### Colour stability

Colour stability was verified using colorimetric measurements before and after 72 h of direct exposure to acidic or alkaline environments (Tables 6 & 7). The total colour variation ( $\Delta E$ ) was calculated using Equation 3 in *ColorMine* software. The CIEL\*a\*b\* system defines three parameters: L\*, a\* and b\*, which represent black/white (lightness), red/green and yellow/blue colour pairs, respectively, and these can be used to evaluate changes in colour due to the physical and chemical properties of various species (Almeida *et al.*, 2021). The CIEL\*a\*b\* system of evaluating colorimetric stability is used because it expresses colour values precisely and numerically, allowing comparison before and after exposure to acidic or alkaline environments in this study (Ezati *et al.*, 2021; Horsth *et al.*, 2023).

In an acidic environment, the RS800 sample showed greater colour variation after 72 h of exposure (at  $\Delta E = 3.16$ ), which is

**Table 5.** Comparison of MB adsorption capacities (mg g<sup>-1</sup>) of the adsorbent from this study and other adsorbents reported previously.

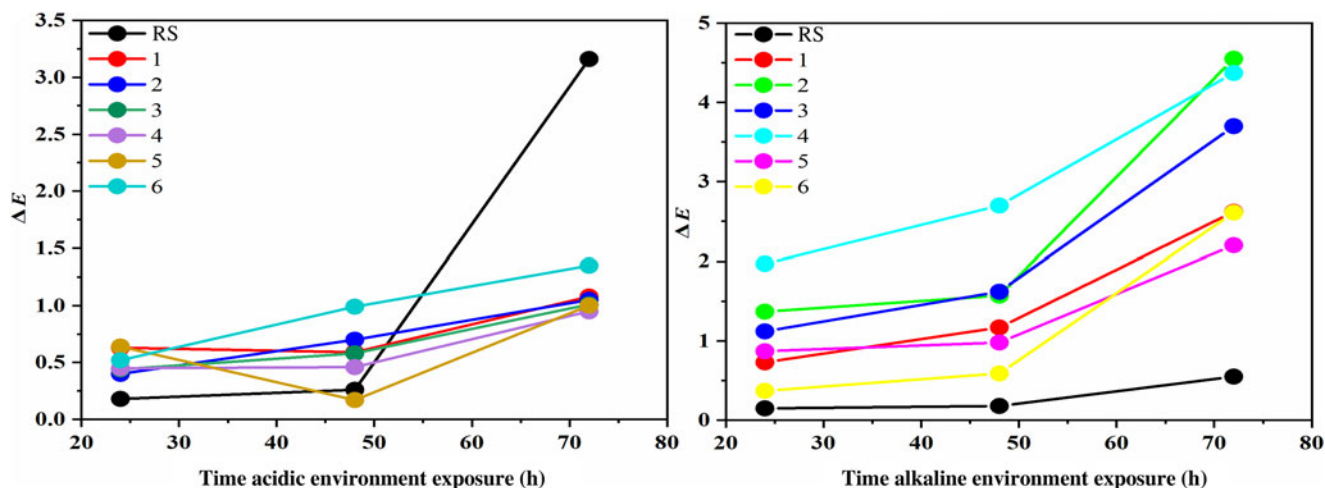
Adsorbent	Adsorption capacity ( $q_{\text{max}}$ ; mg g <sup>-1</sup> )	Reference
Biochar produced from rapeseed, whitewood and seaweed (RS-TC)	14.20	Güleç <i>et al.</i> (2022)
Biochar produced from rapeseed, whitewood and seaweed (RS-HC)	16.10	Güleç <i>et al.</i> (2022)
Sugarcane bagasse	17.43	Meili <i>et al.</i> (2019)
Brown clay	123.50	Munir <i>et al.</i> (2020)
Natural clay	113.63	Bingül (2022)
Chemically modified lychee seed biochar	124.53	Sahu <i>et al.</i> (2020)
RS800	23.25	This study

considered a clear difference (Horsth *et al.*, 2021), and the other samples (Table 6) showed values that represent a very clear colour difference, demonstrating that the adsorption of the dye in the sample provides colour stability to the obtained hybrid pigment. The opposite outcome occurs in an alkaline environment, in which the samples with the adsorbed MB dye demonstrated greater colour variation than pure samples. This behaviour is observed because the dye used is basic (Leon, 1996); therefore, in an alkaline environment, the dye tends to become bluer, demonstrated by a tendency towards negative b\* values, causing greater colour variation (Fig. 11).















### Conclusions

The performance of RS was investigated in terms of its ability to remove MB dye from an aqueous medium as a low-cost alternative for wastewater treatment. The soil was treated thermally at 800°C to remove volatiles, open pores and lamellar spaces. The XRD, EDXRF and FTIR characterization techniques indicate that the RS used contains kaolinite and iron oxides in the form of goethite and hematite.

$\zeta$ -potential measurements indicated a negative surface charge of RS at pH > 4, facilitating its application in the adsorption of cationic dyes. Increasing temperature decreased removal efficiency; therefore, ambient conditions (25°C) were considered

**Figure 11.** Colour stability  $\Delta E$  vs sample exposure time in (a) acidic and (b) alkaline environments according to sample data in Tables 6 and 7.

**Table 6.** Colorimetric parameters of pigments after 72 h in an acidic environment.















Sample	Colorimetric parameters					$\Delta E$	Photograph
	L*	a*	b*	C*	h*		
RS800 (0 h)	76.74	9.63	10.23	14.05	46.73	3.16	
RS800 (72 h)	79.90	9.52	10.19	13.94	46.94		
1 (0 h)	70.84	3.34	3.21	4.63	43.84	1.08	
1 (72 h)	70.90	4.23	2.61	4.97	31.66		
2 (0 h)	66.65	2.28	2.81	3.62	50.95	1.05	
2 (72 h)	66.95	3.22	2.46	4.05	37.34		
3 (0 h)	66.48	1.87	1.82	2.61	44.28	1.01	
3 (72 h)	66.78	2.71	1.34	3.03	26.36		
4 (0 h)	66.42	0.98	0.02	0.99	1.20	0.95	
4 (72 h)	66.59	1.85	-0.33	1.88	350.02		
5 (0 h)	65.68	1.18	-0.39	1.24	341.52	1.00	
5 (72 h)	65.91	2.15	-0.34	2.18	350.93		
6 (0 h)	65.43	0.69	-0.64	0.94	316.92	1.35	
6 (72 h)	66.45	1.58	-0.69	1.73	336.34		

Numbers 1–6 refer to samples resulting from adsorption (Fig. 9) dispersed in ink for acid-base stability testing.

appropriate for its use, removing the need for a heating step, which would make the water-treatment process more expensive.

Colorimetry measurements indicate that, after adsorption, the solids can be used as hybrid pigments. Colour stability tests showed greater stability in acidic environments, while in alkaline

**Table 7.** Colorimetric parameters of pigments after 72 h in an alkaline environment.

Sample	Colorimetric parameters					$\Delta E$	Photograph
	L*	a*	b*	C*	h*		
RS800 (0 h)	75.28	9.70	10.37	14.20	46.93	0.55	
RS800 (72 h)	75.61	9.43	10.03	13.75	46.77		
1 (0 h)	71.26	2.36	2.98	3.80	51.67	2.62	
1 (72 h)	73.10	4.11	2.33	4.72	29.50		
2 (0 h)	70.64	1.86	2.41	3.05	52.36	4.55	
2 (72 h)	74.70	3.86	1.92	4.31	26.5		
3 (0 h)	68.59	2.18	3.21	3.88	55.77	3.70	
3 (72 h)	71.63	4.21	2.62	4.96	31.94		
4 (0 h)	68.18	0.72	0.30	0.78	22.34	4.37	
4 (72 h)	71.87	2.76	-0.84	2.89	343.03		
5 (0 h)	66.84	1.03	0.51	1.15	26.25	2.20	
5 (72 h)	68.19	2.77	0.45	2.81	9.15		
6 (0 h)	65.05	0.18	-0.81	0.83	282.57	2.61	
6 (72 h)	67.10	1.79	-0.82	1.97	335.27		

Numbers 1–6 refer to samples resulting from adsorption (Fig. 9) dispersed in ink for acid-base stability testing.

environments the pigments showed colour variation, suggesting less stability; however, colour variation in the paint could be used as an indicator of a more acidic or a more alkaline environment. The results discussed allow us to propose that this purified and heat-treated RS could be used as an alternative for removing cationic dyes from effluents and could then be used as an

organic–inorganic hybrid pigment for building paints, representing a possible circular economy.

This RS could potentially be diversified by functionalizing it with electron donor or acceptor groups for the selective removal of the metallic ions, phosphate, chlorates and sulfates present in wastewaters, lakes and streams. This RS represents an inexpensive alternative for water treatment.

**Financial support.** DLS thanks CAPES (grant number 88887.628497/2021-00) for a graduate scholarship. FJA thanks CNPq for the following grants: 310815/2022-3 and 427127/2018-1.

## References

- Aksu Z. (2005) Application of biosorption for the removal of organic pollutants: a review. *Process Biochemistry*, **40**, 997–1026.
- Almeida C.A.P., Debacher N.A., Downs A.J., Cottet L. & Mello C.A.D. (2009) Removal of methylene blue from colored effluents by adsorption on montmorillonite clay. *Journal of Colloid and Interface Science*, **332**, 46–53.
- Almeida T.H., Almeida D.H., Gonçalves D. & Lahr F.A.R. (2021) Color variations in CIELAB coordinates for softwoods and hardwoods under the influence of artificial and natural weathering. *Journal of Building Engineering*, **35**, 101965.
- Alver E., Metin A.Ü. & Brouers F. (2020) Methylene blue adsorption on magnetic alginate/rice husk bio-composite. *International Journal of Biological Macromolecules*, **154**, 104–113.
- Anantha M.S., Olivera S., Hu C., Jayanna B.K., Reddy N., Venkatesh K. *et al.* (2020) Comparison of the photocatalytic, adsorption and electrochemical methods for the removal of cationic dyes from aqueous solutions. *Environmental Technology and Innovation*, **17**, 100612.
- Anvari F., Keirikhah M. & Amraei R. (2014) Treatment of synthetic textile wastewater by combination of original article treatment of synthetic textile wastewater by combination of coagulation/flocculation process and electron beam irradiation. *Journal of Community Health Research*, **3**, 31–38.
- Benhachem F.-Z., Attar T. & Bouabdallah F. (2019) Kinetic study of adsorption methylene blue dye from aqueous solutions using activated carbon from starch. *Chemical Review and Letters*, **2**, 33–39.
- Benites V.M., Mendonça E.S., Schaefer C.E.R. & Martin Neto L. (1999) Caracterização dos ácidos húmicos extraídos de um latossolo vermelho-amarelo e de um podzol por análise termodiferencial e pela espectroscopia de absorção no infravermelho. *Revista Brasileira de Ciência do Solo*, **23**, 543–551.
- Bingül Z. (2022) Determination of affecting parameters on removal of methylene blue dyestuff from aqueous solutions using natural clay: Isotherm, kinetic, and thermodynamic studies. *Journal of Molecular Structure*, **1250**, 131729.
- Borth K.W., Galdino C.W., Teixeira V.C. & Anaissi F.J. (2021) Iron oxide nanoparticles obtained from steel waste recycling as a green alternative for Congo red dye fast adsorption. *Applied Surface Science*, **546**, 149126.
- Bortoluzzi E.C., Pernes M. & Tessier D. (2007) Interestratificado caulinita-esmectita em um argissolo desenvolvido a partir de rocha sedimentar do Sul do Brasil. *Revista Brasileira de Ciência do Solo*, **31**, 1291–1300.
- Chaari I., Fakhfakh E., Medhioub M. & Jamoussi F. (2019) Comparative study on adsorption of cationic and anionic dyes by smectite rich natural clays. *Journal of Molecular Structure*, **1179**, 672–677.
- Conama (2005) *Conselho Nacional do Meio Ambiente. Resolução nº 357, 17 de março de 2005, Art. 15-III e Art. 16-I*. Ministério do Meio Ambiente, Brasília, Brazil, 36 pp.
- Cullity B.D. & Stock S.R. (1956) *Elements of X-Ray Diffraction*. Addison-Wesley Publishing Company, Inc., Boston, MA, USA, 555 pp.
- Deotale A.J. & Nandedkar R.V. (2016) Correlation between particle size, strain and band gap of iron oxide nanoparticles. *Materials Today: Proceedings*, **3**, 2069–2076.
- dos Santos H.G. & Zaroni M.J. (2021) Teor de óxidos de ferro. *EMBRAPA (Brazilian Agricultural Research Corporation)*. Available at: <https://www.embrapa.br/en/agencia-de-informacao-tecnologica/tematicas/solos-tropicais/sibcs/classificacao-do-perfil/atributos-diagnosticos/teor-de-oxidos-de-ferro>
- Ezati P., Bang Y.-J. & Rhim J.-W. (2021) Preparation of a shikonin-based pH-sensitive color indicator for monitoring the freshness of fish and pork. *Food Chemistry*, **337**, 127995.
- Fontes M.P.F., de Camargo O.A. & Sposito G. (2001) Eletroquímica das partículas coloidais e sua relação com a mineralogia de solos altamente intemperizados. *Scientia Agricola*, **58**, 627–646.
- Gargori C., Cerro S., Galindo R., García A., Llusar M. & Monrós G. (2012) Iron and chromium doped perovskite (CaMO<sub>3</sub> M = Ti, Zr) ceramic pigments, effect of mineralizer. *Ceramics International*, **38**, 4453–4460.
- Gonçalves M., de Castro C.S., Oliveira L.C.A. & Guerreiro M.C. (2009) Síntese e caracterização de nanopartículas de óxido de ferro suportadas em matriz carbonácea: remoção do corante orgânico azul de metileno em água. *Química Nova*, **32**, 1723–1726.
- Gonçalves D., Leite W.C., Brinatti A.M., Saab S.C., Iarosz K.C., Mascarenhas Y.P. *et al.* (2008) Mineralogia de um latossolo vermelho distrófico submetido a diferentes manejos por 24 anos. *Revista Brasileira de Ciência do Solo*, **32**, 2647–2652.
- Güleç F., Williams O., Kostas E.T., Samson A., Stevens L.A. & Lester E. (2022) A comprehensive comparative study on methylene blue removal from aqueous solution using biochars produced from rapeseed, whitewood, and seaweed via different thermal conversion technologies. *Fuel*, **330**, 125428.
- Hameed B., Din A. & Ahmad A. (2007) Adsorption of methylene blue onto bamboo-based activated carbon: kinetics and equilibrium studies. *Journal of Hazardous Materials*, **141**, 819–825.
- Honorato A.C., Machado J.M., Celante G., Borges W.G.P., Dragunski D.C. & Caetano J. (2015) Biosorption of methylene blue using agro-industrial residues. *Revista Brasileira de Engenharia Agrícola e Ambiental*, **19**, 705–710.
- Horsth D.F.L., Primo J.O., Dalpasquale M., Bittencourt C. & Anaissi F.J. (2021) Colored aluminates pigments obtained from metallic aluminum waste, an opportunity in the circular economy. *Cleaner Engineering and Technology*, **5**, 100313.
- Horsth D.F.L., Primo J.O., Balaba N., Anaissi F.J. & Bittencourt C. (2023) Color stability of blue aluminates obtained from recycling and applied as pigments. *RSC Sustainability*, **1**, 159–166.
- Inda Junior A.V. & Kämpf N. (2005) Variabilidade de goethita e hematita via dissolução reductiva em solos de região tropical e subtropical. *Revista Brasileira de Ciência do Solo*, **29**, 851–866.
- Inyinbor A.A., Adekola F.A. & Olatunji G.A. (2016) Kinetics, isotherms and thermodynamic modeling of liquid phase adsorption of rhodamine B dye onto *Raphia hookeri* fruit epicarp. *Water Resources and Industry*, **15**, 14–27.
- Jaeger S., Dos Santos A., Fernandes A.N. & Almeida C.A.P. (2015) Removal of *p*-nitrophenol from aqueous solution using Brazilian peat: kinetic and thermodynamic studies. *Water, Air, and Soil Pollution*, **226**, 236.
- Ker J.C. (1997) Latossolos do Brasil: uma revisão. *Geonomos*, **5**, 17–40.
- Kumar R.S. & Rajkumar P. (2014) Characterization of minerals in air dust particles in the state of Tamilnadu, India through FTIR, XRD and SEM analyses. *Infrared Physics and Technology*, **67**, 30–41.
- Leon L. (1996) Amperometric flow-injection method for the assay of L-ascorbic acid based on the photochemical reduction of methylene blue. *Talanta*, **43**, 1275–1279.
- Lima J.M., Anderson S.J. & Curi N. (2000) Phosphate-induced clay dispersion as related to aggregate size and composition in hapludoxs. *Soil Science Society of America Journal*, **64**, 892–897.
- Martinelli A.C., Barrada R.V., Ferreira S.A.D., de Freitas M.B.J.G. & Lelis M.F.F. (2014) Evaluation of the leached cadmium and nickel from the degradation of nickel–cadmium batteries in a column of soil. *Química Nova*, **37**, 465–472.
- Meili L., Lins P.V.S., Costa M.T., Almeida R.L., Abud A.K.S., Soletti J.I. *et al.* (2019) Adsorption of methylene blue on agroindustrial wastes: experimental investigation and phenomenological modelling. *Progress in Biophysics and Molecular Biology*, **141**, 60–71.
- Melo V.F. & Alleoni L.R.F. (2009) *Química e Mineralogia do Solo, Parte II – Aplicações*, 1st edition. Sociedade Brasileira de Ciência do Solo, Viçosa, Brazil, 685 pp.
- Moraes É.D.P., Machado N.R.C.F. & Pergher S.B.C. (2003) Síntese da zeólita a partir de um caulim brasileiro termicamente ativado. *Acta Scientiarum. Technology*, **25**, 63–69.

- Morales-Marín A., Ayastuy J.L., Iriarte-Velasco U. & Gutiérrez-Ortiz M.A. (2019) Nickel aluminate spinel-derived catalysts for the aqueous phase reforming of glycerol: effect of reduction temperature. *Applied Catalysis B: Environmental*, **244**, 931–945.
- Moreira S.A., Sousa F.W., Oliveira A.G., Nascimento R.F. & de Brito E.S. (2009) Remoção de metais de solução aquosa usando bagaço de caju. *Química Nova*, **32**, 1717–1722.
- Munir M., Nazar M.F., Zafar M.N., Zubair M., Ashfaq M., Hosseini-Bandegharai A. et al. (2020) Effective adsorptive removal of methylene blue from water by didodecyldimethylammonium bromide-modified brown clay. *ACS Omega*, **5**, 16711–16721.
- Nayl A.A., Abd-Elhamid A.I., Arafa W.A.A., Ahmed I.M., AbdEl-Rahman A.M.E., Soliman H.M.A. et al. (2023) A novel P@SiO<sub>2</sub> nano-composite as effective adsorbent to remove methylene blue dye from aqueous media. *Materials*, **16**, 514.
- Niinimäki K., Peters G., Dahlbo H., Perry P., Rissanen T. & Gwilt A. (2020) The environmental price of fast fashion. *Nature Reviews Earth and Environment*, **1**, 189–200.
- Oladoye P.O., Ajiboye T.O., Omotola E.O. & Oyewola O.J. (2022) Methylene blue dye: toxicity and potential elimination technology from wastewater. *Results in Engineering*, **16**, 100678.
- Oliveira L.C.A., Fabris J.D. & Pereira M.C. (2013) Óxidos de ferro e suas aplicações em processos catalíticos: uma revisão. *Química Nova*, **36**, 123–130.
- Pereira L. & Alves M. (2012) Dyes – environmental impact and remediation. Pp. 111–162 in: *Environmental Protection Strategies for Sustainable Development* (A. Malik & E. Grohmann, editors). Springer, Dordrecht, The Netherlands.
- Quindici M. (2013) *O Segredo das Cores*. All Print Editora, São Paulo, Brazil, 204 pp.
- Rodrigues I.A., Villalba J.C., Santos M.J., Melquiades F.L. & Anaissi F.J. (2020) Smectitic clays enriched with ferric ions for the rapid removal of anionic dyes in aqueous media. *Clay Minerals*, **55**, 12–23.
- Sahu S., Pahi S., Tripathy S., Singh S.K., Behera A., Sahu U.K. & Patel R.K. (2020) Adsorption of methylene blue on chemically modified lychee seed biochar: dynamic, equilibrium, and thermodynamic study. *Journal of Molecular Liquids*, **315**, 113743.
- Shen D., Fan J., Zhou W., Gao B., Yue Q. & Kang Q. (2009) Adsorption kinetics and isotherm of anionic dyes onto organo-bentonite from single and multisolite systems. *Journal of Hazardous Materials*, **172**, 99–107.
- Wang L. (2009) Aqueous organic dye discoloration induced by contact glow discharge electrolysis. *Journal of Hazardous Materials*, **171**, 577–581.
- Xu H. & Van Deventer J.S.J. (2002) Microstructural characterisation of geopolymers synthesised from kaolinite/stilbite mixtures using XRD, MAS-NMR, SEM/EDX, TEM/EDX, and HREM. *Cement and Concrete Research*, **32**, 1705–1716.
- Zhao W., Shi H. & Wang D. (2004) Ozonation of cationic red X-GRL in aqueous solution: degradation and mechanism. *Chemosphere*, **57**, 1189–1199.